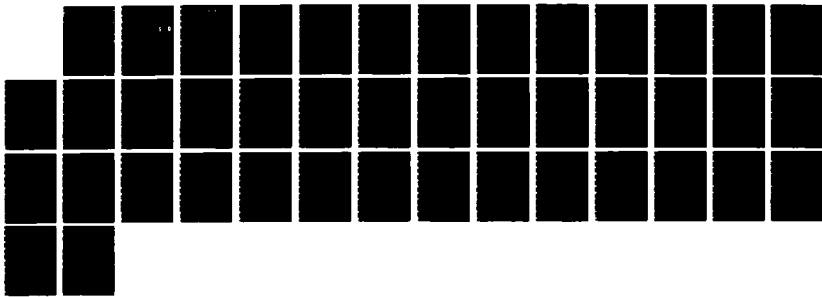
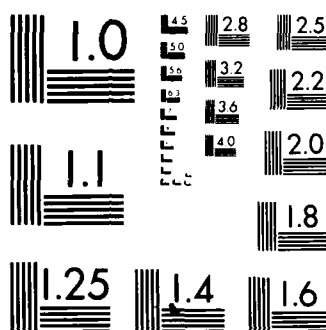


AD-A170 647 FULLY-PLASTIC CRACK GROWTH IN ASYMMETRIC PLANE STRAIN 1/1
BENDING(U) MASSACHUSETTS INST OF TECH CAMBRIDGE DEPT OF
MECHANICAL ENGINEERING F A MCCLINTOCK ET AL 31 JUL 86
UNCLASSIFIED N00014-82-K-0025 F/G 11/6 NL





MICROCOPY RESOLUTION TEST CHART
NATIONAL BUREAU OF STANDARDS-1963-A

DTIC FILE COPY

AD-A170 647

Technical Report N00014-82-K-0025 P00002 TR08

1

FULLY-PLASTIC CRACK GROWTH IN ASYMMETRIC PLANE STRAIN BENDING

Frank A. McClintock

Room 1-304, (617) 253-2219

Francisco J. Wu

Room 3-382, (617) 253-3559

Department of Mechanical Engineering
Massachusetts Institute of Technology
Cambridge, MA 02139

DTIC
SELECTED
S D
AUG 11 1986
D

Unlimited Distribution

31 July, 1986

Technical Report

DISTRIBUTION STATEMENT A

Approved for public release
Distribution Unlimited

Prepared for

OFFICE OF NAVAL RESEARCH

Solids Mechanics Program, Mechanics Division

Scientific Officer: Dr. Yapa Rajapakse

Code 432S (202) 696-4306

800 N. Quincy Street

Arlington, VA 22217

86 3 3 120

REPORT DOCUMENTATION PAGE			READ INSTRUCTIONS BEFORE COMPLETING FORM	
1. REPORT NUMBER N00014-82-K-0025 P00002 TR08		2. GOVT ACCESSION NO. AD-1170641		3. RECIPIENT'S CATALOG NUMBER
4. TITLE (and Subtitle) FULLY PLASTIC CRACK GROWTH ON ASYMMETRIC PLANE STRAIN BENDING		5. TYPE OF REPORT & PERIOD COVERED Technical Report 31 July 1986		6. PERFORMING ORG. REPORT NUMBER
7. AUTHOR(s) Frank A. McClintock Francisco J. Wu		8. CONTRACT OR GRANT NUMBER(s) N00014-82-K-0025 P00002		10. PROGRAM ELEMENT, PROJECT, TASK AREA & WORK UNIT NUMBERS
9. PERFORMING ORGANIZATION NAME AND ADDRESS Department of Mechanical Engineering Massachusetts Institute of Technology Cambridge MA 02139		12. REPORT DATE 31 July 1986		11. CONTROLLING OFFICE NAME AND ADDRESS Office of Naval Research Solid Mechanics Program, Mech. Div. Code 432S 800 N. Quincy St., Arlington, VA 22217
14. MONITORING AGENCY NAME & ADDRESS (if different from Controlling Office)		13. NUMBER OF PAGES 47		15. SECURITY CLASS. (of this report) Unclassified
16. DISTRIBUTION STATEMENT (of this Report) Distribution unlimited		17. DISTRIBUTION STATEMENT (of the abstract entered in Block 20, if different from Report)		15a. DECLASSIFICATION/DOWNGRADING SCHEDULE
18. SUPPLEMENTARY NOTES				
19. KEY WORDS (Continue on reverse side if necessary and identify by block number) Ductile fracture, fully plastic, mixed mode, crack initiation, crack growth, Mode I, Mode II, asymmetry, crack ductility, weld defects, shear band, theory, experiments, crack opening angle, crack tip displacement, steel, HY-80, HY-100, fracture stable design, bending, slip line field, low cycle fatigue				
20. ABSTRACT (Continue on reverse side if necessary and identify by block number) The crack growth ductility of notched parts depends highly on the mode of loading as well as on the geometry. Specimens of symmetrical geometry are commonly tested to predict the plastic behavior of the material under specific loading conditions, but vessels and other structural components often have welds which introduce asymmetric geometry and inhomogeneous properties. In single edge groove, fully-plastic tensile specimens with asymmetries that give a single shear band, a crack can propagate with 1/3 the ductility of				

symmetrical shear bands. Since bending involves more triaxiality, the ductility in asymmetrically grooved cantilever bending is likely to be further reduced, which may lead to an unsafe structure. The triaxiality, slipline geometry, and upper bounds to the limit load are described in detail. Medium strength, low-hardening steels (HY-80 and HY-100) were tested under configurations that showed more triaxiality under one single active slipline field than single edge notch tension specimens.

Two ductility measures were considered: first, a structural crack growth ductility defined as the displacement at the point where the load is applied, per unit of load drop; and second, the local crack growth ductility, defined as the local slip per unit of crack growth. The asymmetrical structural crack growth ductility, as well as the local crack growth ductility were as low as 1/4 of their respective symmetrical crack growth ductilities in HY-80, and in HY-100, asymmetrical structural crack growth ductility was 1/2 the symmetrical one and asymmetrical local crack growth ductility was 1/3 the symmetrical one.

In addition, when the local crack growth ductility in bending specimens is compared to that for single edge grooved tensile specimens, symmetrical bending gives 3/4 the ductility of symmetrical tension specimens, and asymmetrical bending gives 1/2 the ductility of asymmetrical tension specimens.

Thus, asymmetric bending configurations give lower ductilities than symmetric configurations or single edge grooved tension specimens. This should be taken into account in considering the safety of possibly crack structural components and pressure vessels.

Fully-Plastic Crack Growth in Asymmetric Plane Strain Bending

by Frank A. McClintock and F.J. Wu

Abstract

Crack growth ductility on notched specimens depends highly on the mode of loading as well as on the geometry. Specimens of symmetrical geometry are commonly tested to predict the plastic behavior of the material under specific loading conditions but vessels and other structural components often have welds which introduce asymmetric geometry and inhomogeneous properties. In single edge groove, fully-plastic tensile specimens with asymmetries that give a single shear band, a crack can propagate with 1/3 the ductility of symmetrical shear bands (Kardomateas 1985). Since bending involves more triaxiality, the ductility in asymmetrically grooved cantilever is likely to be further reduced, and therefore lead to unsafe structures. The triaxiality, slipline geometry, and upper bounds to the limit load are described in detail. Medium strength, low-hardening steels (HY-80 and HY-100) were tested under configurations that showed more triaxiality under one single active slipline field than single edge notch tension specimens.

Two ductility measures were considered: first, a structural crack growth ductility defined as the displacement at the point where the load is applied per unit of load drop; and second, the local crack growth ductility defined as the amount of local slip per unit of crack growth. The asymmetrical structural crack growth ductility as well as the local crack growth ductility were as low as 1/4 of their respective symmetrical crack growth ductilities in HY-80; and in HY-100, asymmetrical structural crack growth ductility was 1/2 the symmetrical ones and asymmetrical local crack growth ductility was 1/3 the symmetrical ones.

In addition, when the local crack growth ductility in bending specimens is compared to single edge groove tensile specimens, symmetrical bending give 3/4 the ductility of symmetrical tension specimens, and asymmetrical bending give 1/2 the ductility of asymmetrical tension specimens.

Thus, asymmetric bending configurations give lower ductilities than

Codes
d/or
cial

Dist	
A-1	



symmetric configurations or single edge grooved tension specimens. This should be taken into account in considering the safety of possibly cracked structural components and pressure vessels.

Introduction

If a structure cracks, it is desirable that any crack growth be fully plastic to provide large deflections both for stability by load-shedding to other parts of the structure, and simplicity of crack detection before failure of the entire structure. This desired crack growth ductility is reduced by asymmetric geometry that focuses the deformation into a single shear band, along which the crack advances into pre-damaged material, rather than between a pair of sliplines into new material. Such asymmetric geometries occur near welds and fillets in pressure vessels and other structures. Kardomateas (1985) has shown that in asymmetric single-edge notched tensile specimens, crack growth along a single shear band reduces crack growth ductility by a factor of 3 in medium strength alloys with low strain hardening exponents ($n = 0.12$). Even lower ductilities would be expected in bending which gives higher triaxiality, here taken to be the ratio of mean normal stress to the plane strain shear strength, c/k . Green and Hundy (1956) studied bend test specimens as in the Izod (cantilever) and Charpy (three point) bend tests, having either a V groove or a groove whose root is a circular arc. Although the Izod test is non-symmetrical, it has not been instrumented as the Charpy to provide the load-drop description required to calculate crack growth ductility. The question here is the extent to which asymmetry will reduce the crack growth ductility of symmetrical bend specimens.

To express the load-deformation characteristics of a cracked, fully-plastic structure in terms of crack tip singularities or any other local measures would require a fully-plastic stress and strain analysis. In a non-hardening material, slipline analysis applies to both rigid-plastic and elastic-plastic specimens when using strain and displacement increments. The slipline analysis can provide an upper bound to the limit load if the the displacement boundary conditions are

satisfied everywhere across the ligament and the applied load gives positive work. This provides a basis for specimen design and the interpretation of tests, as well as a guide and check for later finite element analysis.

Slipline Analysis

Consider a bar or a plate of rectangular cross-section with a deep, sharp groove on one side (Fig. 1). For ligament-to-depth ratios of less than 1/4, plane strain can be assumed. A weld or heat-affected zone near a crack may produce an asymmetry that can be modelled by adding a shoulder on the back surface of the specimen. The shoulder turns out to force the material to slip only on one of the two sliplines that would occur in the symmetrical geometry.

Slipline analysis gives the fully-plastic non-hardening stress and strain increment distribution. For high strength materials this assumption provides with reasonable estimates of stress distributions. Green (1953) used this analysis for symmetrically grooved rigid-plastic bars under pure bending. Later, Green and Hundy (1956) extended the analysis to three point bend specimens. Here we extend these analyses to a more general asymmetric geometries which could occur near a weld. The generic slipline field is shown in Fig. 2a. It consists primarily of an arc of radius, R_o , where the subscript represents the center of rotation of the arc, across which the assumed rigid material slides as the bend angle is increased. In addition, there may be two fields of constant stress along the groove and back surface, connected to the arc radius R_o by two fans of radii, R_g and R_s . These three variables, together with the angle of the slipline at the tip of the groove, the triaxiality of the field, and the limit load, are the unknowns that must be solved in order to completely describe the state in the fully plastic region. Therefore, in addition to the three equilibrium equations in a two-dimensional problem (2 force equations and 1 moment equation) it is necessary to use slipline theory to provide the remaining three equations.

In slipline analysis, a curvilinear element bounded by two orthogonal α and β sliplines, with mean normal stress, σ , and maximum

shear stress, τ , obeys the Hencky equations of equilibrium (Hill (1985) pp.135-136):

$$d\sigma = 2 k d\phi \text{ along an } \alpha \text{ line,} \quad (1a)$$

$$d\sigma = -2 k d\phi \text{ along a } \beta \text{ line.} \quad (1b)$$

When equations 1a and 1b and the incremental slipline angle across the field are applied to the general slipline field of Fig. 2c the Hencky equations are:

$$\sigma_B = (1 + 2\gamma)/k \quad (2a)$$

$$\sigma_C = -(1 + 2\gamma)/k \quad (2b)$$

$$\gamma = (\pi - 1)/2 - \psi - w_1/2 \quad (2c)$$

Five boundary conditions are then used to solve for the slipline geometry and the stress state of the ligament. The first two are the equilibrium conditions in the two dimensions x, and y:

$$\begin{aligned} Ro [\cos(3\pi/4 - \gamma - w_1) + \cos(3\pi/4 + \psi) + \\ \sigma_B \cos(\pi/4 - \gamma - w_1) + \sigma_C \cos(\pi/4 + \psi)] + \\ Rg [\cos(\pi/4 - \gamma - w_1) + \sigma_B \cos(3\pi/4 - \gamma - w_1)] + \\ Rs [\cos(5\pi/4 + \psi) + \sigma_C \cos(7\pi/4 + \psi)] = 0 \end{aligned} \quad (3)$$

$$\begin{aligned} Ro [\sin(3\pi/4 - \gamma - w_1) + \sin(3\pi/4 + \psi) + \\ \sigma_B \sin(\pi/4 - \gamma - w_1) + \sigma_C \sin(\pi/4 + \psi)] + \\ Rg [\sin(\pi/4 - \gamma - w_1) + \sigma_B \sin(3\pi/4 - \gamma - w_1)] + \\ Rs [\sin(5\pi/4 + \psi) + \sigma_C \sin(7\pi/4 + \psi)] = -P \end{aligned} \quad (4)$$

Then the rotational equilibrium must also be satisfied. The moment, M , taken about the center of arc, BC, can be calculated from the following:

$$\begin{aligned} \sigma_B (Rg^2 + Rg^2) - \sigma_C (Ro^2 + Rs^2) + 2 Ro (Rg + Rs) = \\ = 2 P [L + Ro \cos(3\pi/4 - \gamma - w_1) - Rg \cos(\pi/4 - \gamma - w_1)] \end{aligned} \quad (5)$$

The slipline geometry must satisfy the geometry of the specimen. Therefore, the last two boundary conditions are:

$$Rg \cos(\pi/4 - \gamma - w_1) + Rg \cos((5\pi/4 + \psi) - \\ - Rg [\cos(3\pi/4 - \gamma - w_1) + \cos(3\pi/4 + \psi)] = g \quad (3)$$

$$Rg \sin(\pi/4 - \gamma - w_1) + Rg \sin((5\pi/4 + \psi) - \\ - Rg [\sin(3\pi/4 - \gamma - w_1) + \sin(3\pi/4 + \psi)] = -n \quad (4)$$

Equations 3 to 7 apply only until one of the constant stress regions disappears. Further analysis requires deriving the equations governing the shape of the slipline and the magnitude of the load for the new field. The special case of symmetrical grooved bars with no shoulder restriction on the back surface of the specimen was analyzed by Green (1953). His result was used to check the above equations.

Figures 3a and 3b show the two possible sliplines that can occur in a bending specimen with a shoulder in the back surface. The possibility of the constant stress field to appear at the surface of the shoulder instead of at the back surface was analyzed, but the displacement boundary conditions were satisfied only for a shoulder flank angle, w_3 , greater than 0.314 radians (Fig. 2c). From the numerical analysis, the slipline of Fig. 3a turned out to require a lower upper bound to the limit load and therefore was named 'active field'. The slipline in Fig. 3b was the called 'inactive field'. The fields are governed by the groove flank angles, the shoulder distance to the centerline, and the moment arm of the applied load. For the geometry in Fig. 3a the active field shows no constant stress field at the tip of the notch. For this special case where $Rg = 0$, the Hencky equations are:

$$\sigma_b = -(1 + 2\psi + 2\chi) \quad (8a)$$

$$\sigma_c = -(1 + 2\psi) \quad (8b)$$

The equilibrium equations (Eqs. 3 and 4) reduce to:

$$Rg [\cos(\chi + \psi - \pi/4) + \cos(3\pi/4 + \psi) + \\ \sigma_b \cos(\chi + \psi - 3\pi/4) + \sigma_c \cos(\pi/4 + \psi)] + \\ Rg [\cos(5\pi/4 + \psi) + \sigma_c \cos(7\pi/4 + \psi)] = 0 \quad (9)$$

$$\begin{aligned}
 & Ro [\sin(\chi + \psi - \pi/4) + \sin(3\pi/4 + \psi) + \\
 & \sigma_b' \sin(\chi + \psi - 3\pi/4) + \sigma_c \sin(\pi/4 + \psi)] + \\
 & Re [\sin(5\pi/4 + \psi) + \sigma_c \sin(7\pi/4 + \psi)] = -\beta
 \end{aligned} \quad (10)$$

and the moment equation to:

$$\begin{aligned}
 \sigma_b' R_c^2 - \sigma_c (R_b^2 + R_c^2) + 2 Ro Re = \\
 = 2 + \beta L - Ro \cos(\chi + \psi - \pi/4)
 \end{aligned} \quad (11)$$

Simplifying the geometry of the slipline to only to slip arcs. Eqs. 6 and 7 reduce to:

$$Re \cos(5\pi/4 + \psi) - Ro [\cos(\chi + \psi - \pi/4) + \cos(3\pi/4 + \psi)] = 5 \quad (12)$$

$$Re \sin(5\pi/4 + \psi) - Ro [\sin(\chi + \psi - \pi/4) + \sin(3\pi/4 + \psi)] = -h \quad (13)$$

In addition, the initial angle of the slipline at the tip of the groove λ_s can be found geometrically from the relation:

$$\lambda_s = 3\pi/4 - \psi - \chi \quad (14)$$

Equations 8 - 14 were solved numerically for the slipline geometry, as well as the mean normal stress, σ_m , and the limit load, P , for different cantilever lengths, L/h , and shoulder offsets, g/h . Table 1 describes the variation of the normalized load, P/k , maximum mean normal stress, σ/k , and radii, R/h , as a function of the normalized shoulder distance, g/h , for the two possible slipline fields. The regions of constant stress decrease as the shoulder distance from the centerline is increased. The limit load ratio decreases (as desired) as the moment arm is decreased, but at the expense of a decrease of triaxiality. Table 2 describes the slipline behavior, load, and maximum mean normal stress as a function of the moment arm. The criterion used to promote slip by only one field was to have the limit load of any possible field be higher than that of the lowest limit load to overcome strain hardening. The ratio of

$$\frac{(P/kbh)_{\text{lowest}}}{(P/kbh)_{\text{other}}} = \frac{\text{Yield Strength}}{\text{Tensile Strength}}$$

(15)

was assumed first and found to be sufficient.

Figures 4 and 5 describe the effects of shoulder distance and moment arm respectively on the normalized load, mean normal stress, and geometry of the active slipline field. In addition, the ratio of limit load according to Eq. 15 is plotted in Figs. 4a and 5a.

For the special case of asymmetrically grooved specimens under pure bending (Fig. 6) the analysis showed that the limit moment for the inactive field was only 3% more than that for the active field.

Nevertheless, changing the groove flank angles to provide a highest ratio of limit moments would increase the ratio of inactive to active limit moments only to 5%. Strain hardening would overcome this small difference and cause deformation on both sliplines. In addition, the mean normal stress is smaller than for symmetrically grooved specimens, and decreases as the shoulder distance increases. Preliminary experiments on asymmetric pure bend specimens showed that two fields were active. Table 3 gives the normalized limit moment and the normalized mean normal stress for the two slipline fields as the shoulder distance from the centerline, g/b , is varied from -0.2 to 0.7. Preliminary experiments of asymmetrical geometry under pure bending verified the theory by showing very pronounced yielding on both slip planes and no reduction in ductility relative to symmetric specimens. These results led to the above analysis for the cantilever beam loading type.

The experiments on cantilever bars provide an extension to the studies of non-symmetrical specimens in a three point bend done by Green and Hundy (1956) with the standard Izod test by describing the geometry effects on load drop ductility.

Fracture Analysis Interpretation

Crack growth is a mixture of sliding off and fracture. For symmetrical bending specimens it may be idealized by assuming cycles of alternate sliding on two slip-planes and fracture at the tip of the notch

with the microscopic crack propagating at an angle and macroscopically parallel to the ligament, as described in Fig. 7a. In asymmetrical notched specimens, on the other hand, the crack advances into the pre-strained material in the general direction of the dominant slipline field, as shown in Fig. 8a. The ligament reduction is not equivalent to the crack growth as in the symmetrical case, or as in single grooved tension. For practical purposes, a 'structural crack growth ductility' $d\sigma_p/dP$ is defined as the minimum displacement at the point where the load is applied per unit drop in applied load. A more fundamental understanding is given by the 'local crack growth ductility', defined as the crack growth per unit of slip. For symmetrical specimens, Broek (1983) suggests the use of a clip gauge to measure the crack opening displacement (COD). This value can be used to find an approximate value of crack tip opening displacement (CTOD) and stress intensity factor σ_I . Kanninen and Popelar (1985) review the COD and CTOD methods to study the crack growth on symmetrical specimens under three point bend for elastic-plastic materials. They defined the term, (dJ/ds) , as the change of J per unit of crack advance at a specific load point displacement. This term though has significance for a non-linearly elastic material can not be applied to fully-plastic problems. Slipline theory is the most appropriate method for describing the stress distributions across the fully-plastic ligament.

a) Asymmetrical specimens. When the crack propagates along a single shear band, as in the case of asymmetrical grooved cantilever bars, (Fig. 8a) the local crack growth ductility $(Dg_{loc})_s$ is defined as the amount of slip, du_s , per unit of reduction of ligament, dh .

$$(Dg_{loc})_s = du_s/dh \quad (16)$$

On the other hand, the structural crack growth ductility can be defined in terms of normalized displacement per unit of load drop. This quantity is found from experiments by plotting the displacement at the point of applied load, du_p , normalized by the original ligament, h_0 , against the load drop ductility, normalized by the maximum load.

$$(D^0_{\text{str}})_a = \frac{du_p}{dP} = \frac{h_s}{P_{\text{MAX}}} \cdot \frac{du_p/h}{dP/P_{\text{MAX}}} \quad (17)$$

The first term of Eq. 17 is the ratio of the original ligament to the experimental maximum load and the second term is the maximum slope of the falling part of the load-displacement curve.

The relation between this measure of structural behavior to the local crack growth is accomplished by defining each term of the structural crack growth ductility. First, the displacement at the applied load can be described as follows: if R_p is the distance between points O and Q with angle λ_p from the horizontal (Fig. 8b), then:

$$A_p = \frac{R_o \sin \lambda_s + L}{\cos \lambda_p} \quad (18)$$

$$\text{where: } \lambda_p = \text{Arctan} \frac{R_o \cos \lambda_s + a}{R_o \sin \lambda_s + L} \quad (19)$$

then the displacement at the point where the load is applied:

$$\begin{aligned} du_p &= R_p \cos \lambda_p d\theta = (R_o \sin \lambda_s + L) d\theta \\ &= (\sin \lambda_s + L/R_o) R_o d\theta \end{aligned} \quad (20)$$

The amount of slip can be calculated from the slipline arc radius, R_o , and the bend angle θ :

$$du_s = R_o d\theta \quad (21)$$

Substituting Eq. 21 into 20 we get:

$$du_p = (\sin \lambda_s + L/R_o) du_s \quad (22)$$

From slipline analysis the normalized limit load was found to be a function of both normalized shoulder distance to centerline, a/h , and moment arm, L/h . In order to relate the structural and local crack growth ductility it is important to describe the normalized applied load.

From slipline analysis this quantity was found to be a function of the shoulder distance to centerline and moment arm:

$$P/kbh = P/kbh \left(\frac{L}{h}, \frac{g}{h} \right) \quad (23)$$

Differentiating this function we get:

$$\frac{dP}{kbh} = \frac{(\partial P/kbh)}{(\partial g/h)} d(g/h) + \frac{(\partial P/kbh)}{(\partial L/h)} d(L/h) \quad (24)$$

The values of the two derivatives of the normalized load in the right side of equation 24 are determined from the slipline analysis (Table 4). From Fig. 85 the change of normalized shoulder distance, $d(g/h)$ can be described as follows:

$$\begin{aligned} d(g/h) &= \frac{g - dg}{h - dh} - \frac{g}{h} = \frac{g - dh/\tan\lambda}{h - dh} - \frac{g}{h} = \\ &= g/h \left(1 - \frac{dh}{g \tan\lambda} \right) (1 + dh/h) - g/h \end{aligned}$$

As a result:

$$d(g/h) = (g/h - \text{Cot}\lambda) dh/h \quad (25a)$$

and similarly:

$$d(L/h) = (L/h - \text{Cot}\lambda) dh/h \quad (25b)$$

where:

$$\text{Cot}\lambda = \frac{\cos\lambda_s + dc/du_s \cos\lambda_c}{\sin\lambda_s + dc/du_s \sin\lambda_c} \quad (26)$$

Substituting Eqs. 25 into 24:

$$\frac{dP}{kbh} = \frac{\partial P/kbh}{\partial (g/h)} (g/h - \text{Cot}\lambda) + \frac{\partial P/kbh}{\partial (L/h)} (L/h - \text{Cot}\lambda) \frac{dh}{bh} \quad (27)$$

and

$$\frac{dP}{P_{\max}} = \frac{dP}{kbh} \frac{kbh}{P_{\max}} = \frac{dP}{kbh} \frac{kbh_0}{P_{\max}} \frac{h}{h_0} =$$

$$= \frac{\partial P/kbh}{\partial (g/h)} (g/h - \text{Cot}\lambda) + \frac{\partial P/kbh}{\partial (L/h)} (L/h - \text{Cot}\lambda) \frac{kbh_0}{P_{\max}} \frac{dh}{h_0} \quad (28)$$

Finally, substituting equations 22 and 28 into the structural crack growth ductility (Eq. 16) we get:

$$\frac{du_s}{dP} = \frac{(sin \lambda_s + L/h h/R)^{1/2} / k}{\frac{\partial P/kbh}{\partial (g/h)} (g/h - \text{Cot}\lambda) + \frac{\partial P/kbh}{\partial (L/h)} (L/h - \text{Cot}\lambda)} \frac{du_s}{dh} \quad (29)$$

Equation 29 is the general identity relating structural to local crack growth ductility. The parameters in this equation can be found from the previously described slipline analysis and experimental load-displacement curve with the exception of λ which is defined in Eq. 26. This parameter, λ , depends on the microscopic amount of slip, du_s , amount of fracture, dc , and angle of fracture, λ_c . At this point, since the angle of slip, λ_s , is known we assume that fracture occurs at the same orientation as the slip:

$$\lambda_c = \lambda_s \quad (30)$$

then from Eq. 26:

$$\lambda = \lambda_s \quad (31)$$

and Eq. 29 becomes:

$$\frac{du_F}{dP} = \frac{\frac{(\sin \lambda_s + L/h \cdot h/R_o)/kb}{\partial P/kbh} \frac{du_s}{dh}}{\frac{\partial P/kbh}{\partial (g/h)} (g/h - \operatorname{Cot} \lambda_s) + \frac{\partial P/kbh}{\partial (L/h)} (L/h - \operatorname{Cot} \lambda_s)} \quad (32)$$

Let F_g be the geometry factor involving values from the slipline analysis.

$$F_g = \frac{\frac{(\sin \lambda_s + L/h \cdot h/R_o)}{\partial P/kbh} \frac{du_s}{dh}}{\frac{\partial P/kbh}{\partial (g/h)} (g/h - \operatorname{Cot} \lambda_s) + \frac{\partial P/kbh}{\partial (L/h)} (L/h - \operatorname{Cot} \lambda_s)} \quad (33)$$

then

$$(du_F/h_o)/(dP/P_{max}) = (P_{max}/kbh_o) F_g (du_s/dh) \quad (34)$$

or

$$(Dg_{str})_s = F_g / kb (Dg_{loc})_s \quad (35)$$

The value of the geometry factor, F_g , is plotted in Fig. 9 against the normalized moment arm, L/h , for various shoulder distances, g/h .

b) Symmetrical specimens. For the local crack growth ductility on symmetrical specimens, $(Dg_{loc})_s$ is defined as the crack tip opening displacement per unit of crack growth, which is in this case equivalent to the negative of the ligament reduction (Fig. 7a):

$$(Dg_{loc})_s = \frac{d(\text{CTOD})/2}{-dh} = \operatorname{Tan}(\text{COA}/2) \quad (36)$$

where:

$$d(\text{CTOD}) = 2 \cos \lambda_s du_s \quad (37)$$

In symmetrical, pure bend specimens the structural crack growth ductility is defined in terms of the displacement per load drop. The load is characterized by the moment arm, L_a , in which for four point

bending it is defined as the distance between the opposing loads (Fig. 7b):

$$(R_{\text{str}})_{\text{s}} = du_p/dP \quad (38)$$

$$\text{where } du_p = (\sin \lambda_s + L/R_p) R_p d\theta \quad (39)$$

$$\text{and } dP = d\theta/L_s \quad (40)$$

then,

$$(R_{\text{str}})_{\text{s}} = \frac{(\sin \lambda_s + L/R_p) R_p L_s}{M_{\text{max}}} \frac{d\theta}{dM/M_{\text{max}}} \quad (40)$$

The numerator of the first term of Eq. 39 derives from slipline analysis second term is found by calculating the maximum slope of the falling part of the moment-bend angle curve, which is plotted from experiments.

In order to relate structural to local crack growth ductility in symmetrical specimens we need to describe the new introduced pure moment, M , which can be achieved by four point bending. For a fully-plastic ligament a lower bound moment is obtained by assuming a stress distribution satisfying equilibrium equations and nowhere exceeds yielding:

$$M = 2k_b h^2/4 \quad (41)$$

differentiating we get:

$$dM = k_b h dh \quad (42)$$

$$\text{then } \frac{d\theta}{dM/M_{\text{max}}} = \frac{du_s/R_p}{k_b h/M_{\text{max}}} \frac{\cos \lambda_s}{dh} \quad (43)$$

Finally, substituting Eqs. 37 and 43 into 40 the structural crack

growth ductility leads to:

$$\begin{aligned} (\delta_{\text{estr}})_s &= \frac{(\sin\lambda_s + L/R_s) La}{kbh \cos\lambda_s} \frac{d(\text{CTOD})/2}{dh} \\ &= \frac{(\sin\lambda_s + L/R_s) La/h}{kb \cos\lambda_s} (\delta_{\text{loc}})_s \end{aligned} \quad (44)$$

Knowing the structural crack growth ductility of an experiment, the local crack growth ductility can be estimated by the use of Eq. 44 for symmetrical specimens and Eq. 35 for asymmetrical specimens. These equations provide a relation between macroscopically measurable parameters and microscopically crack behavior which can then be used to compare to other types of experiments like the single edge groove tensile tests (McClintock and Kardomateas 1986).

Experiments and Results

a) General description. Asymmetric notched rectangular bars were tested under cantilever and pure bending. The geometry was taken from the results of the slipline analysis that gave the most triaxial state with a reasonable assurance of only one active slipline.

Rectangular bars of HY-80 and HY-100 were used in the bending tests as typical of high strength low alloy structural steels. In addition, these low hardening materials are more appropriate for verifying the analysis using the slipline theory. The tensile behavior of these alloys is listed in Tables 5 and 6 respectively. The geometry of the specimens, taken from the slipline analysis, is described in Fig. 3. In addition, Tables 5 and 6 give the experimental results in a tabulated form.

Stability of the tests was an important consideration due to the expected higher crack growth rate for the asymmetrical case. It was therefore required to design the bending fixtures with the least deflection per unit load. Preliminary tests to determine overall compliances gave values of 1.08×10^{-6} and 6.71×10^{-6} mm/N for the machine and

fixtures respectively.

b) Results. A typical load-displacement curve is shown in Fig. 10; the test procedure was first to produce a low-cycle fatigue initiation crack, of one cycle, at the tip of the notch followed by a monotonic bending load for the crack growth from which data was taken. Again, the results are summarized in Table 5.

Maximum load reached on the first cycle. The load is normalized by the value calculated from the slipline analysis using $k = T_0/\sqrt{2}$. For the symmetrical case, the experimental value agreed to 16% of the analytical while for the asymmetrical cases the values were 43% greater than the analytical.

Plastic angular deflection on low cycle fatigue. The idea behind this low cycle fatigue crack initiation was to produce enough plastic strain to initiate the crack without fatiguing the ligament. In most cases, the structure is subject to similar repeated loads before fracture rather than being subject to high cycle fatigue followed by an overload. Low cycle fatigue seems to produce a crack initiation into the direction of the numerically calculated slipline angle.

The idealised crack initiation displacement, is defined as the difference in between the extension of the steepest part of the loading curve to the maximum load (point A of Fig. 10), and the displacement at maximum load (point B). This quantity is a convenient measure of initiation and can be used to compare with the initiation displacement measured from the fracture surface profiles through a stereo microscope.

Structural crack growth ductility. For a measure of crack growth resistance, the structural crack growth ductility is obtained from the experiments by calculating the steepest slope of the falling part of the load displacement curve. From the design point of view, the structural crack growth ductility, D_{str} , (Eq. 17) describes the physical behavior of the structure. In HY-80 (Fig. 5), the asymmetric bending specimens give 1/4 the load drop ductility of symmetrical specimens while for HY-100 (Fig. 6) the asymmetric specimens give only 1/2 the load drop ductility of symmetrical ones. This reduction of structural ductility, although is not as critical as for the tension tests, is significantly important and should be considered to avoid possible catastrophic

failures.

Local crack growth ductility. In bending local crack growth ductility, as defined in Eq. 16 for asymmetrical specimens and in Eq. 36 for symmetrical ones, can be derived from structural data according to Eqs. 35 and 44 respectively. For a shoulder distance to centerline, $g/h = 0$, asymmetrical HY-80 specimens give 1/3 the local crack growth ductility of symmetrical ones while asymmetrical HY-100 specimens give 1/4 the ductility of symmetrical ones. When the shoulder distance to the centerline increases, the ratio of slip to fracture increases as expected since the triaxiality decreases with increasing g/h . Assuming that the fracture angle, λ_c , was the same as the slip angle, λ_s , HY-80 asymmetric specimens with $g/h = 0.5$ give a ratio of slip to fracture, $d_{us}/dc = 3.5$ while with $g/h = 0$ there is barely any slip compared to fracture.

Conclusion

In low-hardening asymmetric bending specimens, the structural crack growth ductility is 1/4 of the symmetric ones. On the other hand, local crack growth ductility depends on the triaxiality of the ligament. For backsurface shoulder distances, $g/h = 0$, the asymmetric specimens give 1/4 the ductility of symmetrical ones and as the shoulder distance increases triaxiality decreases, and therefore local crack growth ductility increases up to 7 times the symmetrical ones at $g/h = 0.5$.

The limit load calculated numerically was found to agree with experiments with 3% error for symmetrical specimens and 29% error for asymmetrical specimens.

Acknowledgements

We would like to express our thanks to Arthur Rudolph and Bill Henry for the great job in machining the specimens. Also, express our gratitude to A. Wiggs of DTNSRDC for providing with the HY-80 and HY-100 steel, here used in the bending experiments. Special thanks to the

project monitor, Dr. Y. Rajapakse for being enthusiastic about this work, and we give acknowledgement and thanks to the Office of Naval Research, Solid Mechanics Program, Contract N00014-82-K-0025 for sponsoring this exciting research.

References

Broek, D. (1984) 'Elementary Engineering Fracture Mechanics', Martinus Nijhoff Publishers, The Hague.

Ewing, R.J.P. (1968) 'Calculations on the Bending of Rigid/Plastic Notched Bars', 'Journ. of Mech. and Phys. of Solids', v16, pp.205-218.

Green, A.P. (1951) 'The Plastic Yielding of Notched Bars Due to Bending', 'Quart. Journ. Mech. and Applied Math.', v6, pt.2, 223-239.

Green, A.P. and Hundy, B.P. (1956) 'Initial Plastic Yielding in Notch Bend Tests', 'Journ. of Mech. and Phys. of Solids', v4, pp.123-144.

Hill, R. (1955) 'The Mathematical Theory of Plasticity', Clarendon Press, Oxford.

Honaninen, H.P. and Popelar, C.S. (1985) 'Advanced Fracture Mechanics', Oxford University Press Inc., N.Y.

Kardomateas, G.A. (1985) 'Mixed Mode I and II Fully Plastic Crack Growth from Simulated Weld Defects'. PhD thesis, Mechanical Engineering Dept., MIT, (1985).

McClintock, F.A. (1971) 'Plasticity Aspects of Fracture', 'Fracture', v3, H. Liebowitz ed., Academic Press, New York.

McClintock, F.A. and Argon, A.S. (1966) 'Mechanical Behavior of Materials', Addison-Wesley Publishing Company Inc., Reading, Massachusetts.

TABLE 1. Load, Stress, and Radii for Active and Inactive Fields in a Cantilever Bar as a function of the Shoulder Distance g/h .

For a moment arm $l/h = 2$.

Table 1a. Active Field

<u>0.0 < g/h < 0.7</u>		
Load	$0.2976 < P/kbh < 0.5327$	
Stress	$2.2005 > \sigma/k > 1.6575$	
Rad Top	$0.0 = Rg/h = 0.0$	
Rad Ctr	$0.5241 < Ro/h < 0.7473$	
Rad Bot	$0.2764 > Rs/h > 0.0516$	

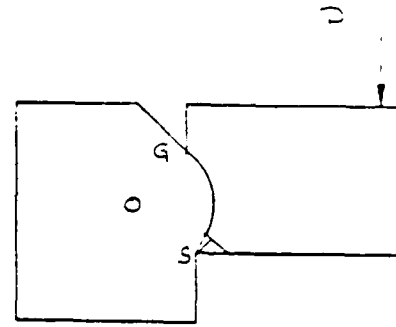
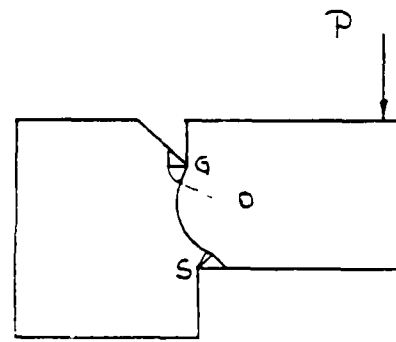


Table 1b. Inactive Field

<u>0.0 < g/h < 0.3870</u>		
Load	$0.3566 < P/kbh < 0.4809$	
Stress	$2.3562 = \sigma/k = 2.3562$	
Rad Top	$0.2003 > Rg/h > 0.0565$	
Rad Ctr	$0.3835 < Ro/h < 0.5462$	
Rad Bot	$0.1983 > Rs/h > 0.0$	



<u>0.3870 < g/h < 0.5980</u>		
Load	$0.4809 < P/kbh < 0.6055$	
Stress	$2.3562 < \sigma/k < 2.4763$	
Rad Top	$0.0565 > Rg/h > 0.0$	
Rad Ctr	$0.5462 < Ro/h < 0.5963$	
Rad Bot	$0.0 = Rs/h = 0.0$	

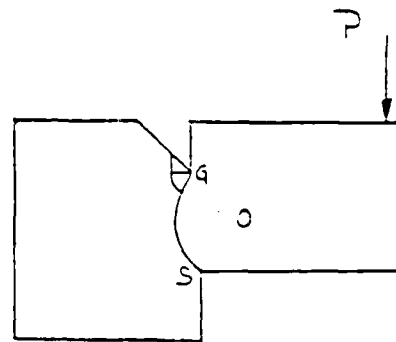


TABLE 2. Load, Stress, and Radii for Active and Inactive Fields in a Cantilever Bar as a Function of the Moment Arm l/h

For a shoulder distance $g/h = 0.0$

Table 2a. Active Field.

$3.0 < (l/h) < 3000$

Load	$0.2606 > (P/kbh) > 0.0026$
Stress	$2.0650 < (\sigma/k) < 2.5001$
Rad Top	$0.0 = (Rg/h) = 0.0$
Rad Ctr	$0.5995 > (Ro/h) > 0.5440$
Rad Bot	$0.1677 < (Rs/h) < 0.2371$

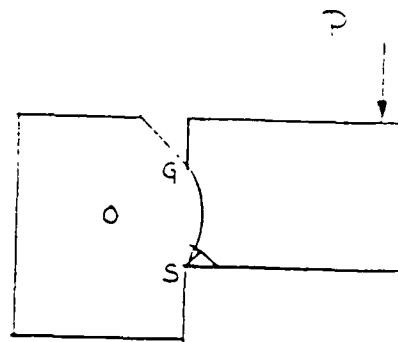


Table 2b. Inactive Field.

$3.0 < (l/h) < 3000$

Load	$0.2335 > (P/kbh) > 0.0002$
Stress	$2.3522 = (\sigma/k) = 2.3522$
Rad Top	$0.1669 > (Rg/h) > 0.0967$
Rad Ctr	$0.4043 < (Ro/h) < 0.4493$
Rad Bot	$0.1891 > (Rs/h) > 0.1752$

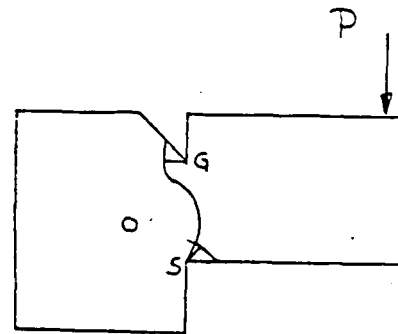
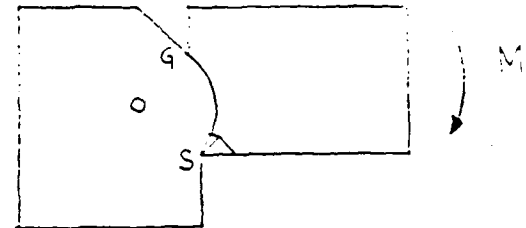


TABLE 3a. Moment, Stress, and Radii for Y earsid. Field
in a Pure Bend Test as a Function of the Shoulder Distance
 g/h for a Flank Angle $w = 0$.

<u>$-0.2 < g/h < 0.3989$</u>		
Moment	$1.2606 < 2M/kbh^2 < 1.5770$	
Stress	$3.0855 > \sigma/k > 2.5010$	
Rad Top	$0.0 = Rg/h = 0.0$	
Rad Ctr	$0.3886 < Ro/h < 0.5442$	
Rad Bot	$0.5027 > Rs/h > 0.2373$	



<u>$0.3989 < g/h < 0.7$</u>		
Moment	$1.5770 < 2M/kbh^2 < 2.0488$	
Stress	$2.5010 > \sigma/k > 2.2551$	
Rad Top	$0.0 < Rg/h < 0.0483$	
Rad Ctr	$0.5442 < Ro/h < 0.6439$	
Rad Bot	$0.2373 > Rs/h > 0.1653$	

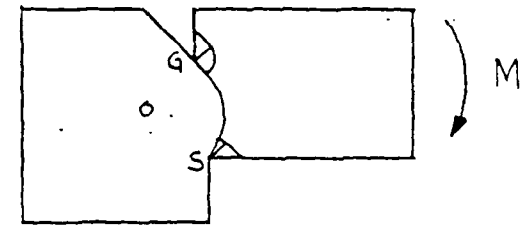
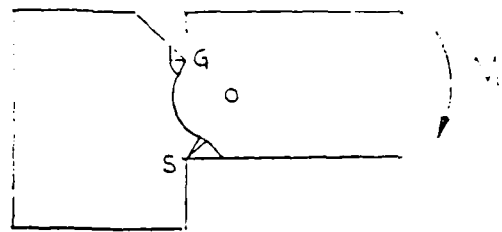
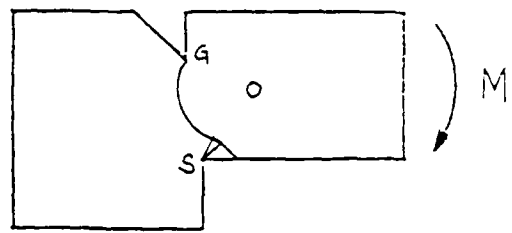


TABLE 3b. Moment, Stress, and Radii for Farside Field in a Pure Bend Test as a Function of the Shoulder Distance g/h for a Flank Angle $w = 45^\circ$.

$w = 45^\circ$	$-0.201 < g/h < 0.2756$
Moment	$1.2680 < 2M/kbh^2 < 1.4847$
Stress	$2.3562 = \sigma/k = 2.3562$
Rad Top	$0.1491 > Rg/h > 0.0$
Rad Ctr	$0.3856 < Ro/h < 0.5592$
Rad Bot	$0.3028 > Rs/h > 0.0103$



$0.2756 < g/h < 0.2934$	
Moment	$1.4847 < 2M/kbh^2 < 1.4989$
Stress	$2.3562 > \sigma/k > 2.3311$
Rad Top	$0.0 = Rg/h = 0.0$
Rad Ctr	$0.5592 < Ro/h < 2.5670$
Rad Bot	$0.0103 > Rs/h > 0.0$



$0.2934 < g/h < 0.7$	
Moment	$1.4989 < 2M/kbh^2 < 2.0563$
Stress	$2.3311 = \sigma/k = 2.3311$
Rad Top	$0.0 = Rg/h = 0.0$
Rad Ctr	$2.5670 < Ro/h < 0.6641$
Rad Bot	$0.0 = Rs/h = 0.0$

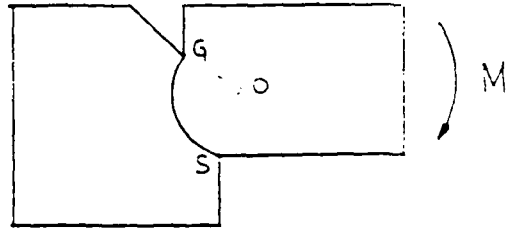


Table 4a. Geometry as a function of shoulder distance to crack tip

q/h	L/h	P/kbh	Psi	Gamma	o/k	Lamda	Ro/h	Rc/h
.218	2	.28786	0	1.7440	2.488024	.61218	.470250	.388406
.2	2	.28792	.01137	1.7411	2.459379	.60377	.475443	.388336
.1	2	.29054	.07106	1.7319	2.321628	.55327	.499465	.328039
0	2	.29758	.13162	1.7319	2.200553	.49267	.524117	.210483
.1	2	.30982	.19206	1.7395	2.094787	.42468	.549759	.231266
.2	2	.32802	.25139	1.7526	2.002340	.35225	.576866	.191612
.3	2	.35289	.30578	1.7692	1.920851	.27821	.605910	.156897
.4	2	.38511	.36362	1.7875	1.847256	.20502	.637276	.126245
.5	2	.42536	.41554	1.8060	1.780993	.13462	.671225	.098898
.6	2	.47434	.46440	1.8235	1.718140	.06832	.707894	.074199
.7	2	.53277	.51026	1.8390	1.657479	.00694	.747316	.051611

Table 4b. Geometry as a function of moment arm

q/h	L/h	P/kbh	Psi	Gamma	o/k	Lamda	Ro/h	Rc/h	2M/kbh
0			.11247	2.0203	2.815652	.22342	.434485	.390677	1.2892210
0	10000	6.4E-5	.11248	2.0202	2.815524	.22348	.434499	.390656	1.2892210
0	1000	6.4E-4	.11252	2.0197	2.814366	.22397	.434620	.390474	1.2892212
0	100	.00644	.11297	2.0144	2.802795	.22886	.435841	.388647	1.2892378
0	10	.06376	.11723	1.9609	2.687400	.27804	.448849	.369834	1.2905640
0	5	.12582	.12153	1.9018	2.560610	.33282	.465021	.347844	1.2964389
0	4	.15607	.12351	1.8726	2.498136	.36011	.473788	.336456	1.3006770
0	3	.20515	.12654	1.8245	2.395878	.40517	.489391	.316964	1.3100701
0	2	.29758	.13162	1.7319	2.200553	.49267	.524117	.276463	1.3378485
0	1.6	.36126	.13462	1.6667	2.064097	.55491	.552883	.245268	1.3664924
0	1.4	.40359	.13637	1.6227	1.972664	.59712	.574601	.222844	1.3906155
0	1.2	.45586	.13826	1.5678	1.859053	.65015	.604730	.193082	1.4277885
0	1	.52119	.14017	1.4983	1.716171	.71777	.648376	.152290	1.4868229

Table 4c. Geometry as a function of moment arm

q/h	L/h	P/kbh	Psi	Gamma	o/k	Lamda	Ro/h	Rc/h	2M/kbh
.5	2	.42536	.41554	1.8060	1.780993	.13462	.671225	.098898	1.7780716
.5	1.8	.47013	.42048	1.7725	1.706017	.16222	.685873	.083888	1.7966064
.5	1.6	.52466	.42640	1.7332	1.613704	.19655	.705377	.064489	1.8234606
.5	1.4	.59211	.43353	1.6826	1.498052	.24010	.732335	.038642	1.8641496
.5	1.2	.67675	.44220	1.6175	1.350651	.29647	.771317	.002955	1.9291693
.5	1	.78400	.45266	1.5328	1.160287	.37072	.830755	-.04832	2.0399176

TABLE 5a. Ambient temperature mechanical properties of HY-80 steel.

Composition: 0.18% C, 2-3.25% Ni,
0.10-0.40% Mn,
0.15-0.35% Si

Properties:	Yield Strength MN/m ²	Tensile Strength MN/m ²	Hardness HBN kgf/mm ²	Reduction in area %
	587	692	175	69.9

TABLE 5b. Experimental results

(l/h = 2.0)	Sym.	Asymmetrical		
(g/h)		0.0	0.5	0.5
ligament size (mm)	10.41	10.79	10.67	10.54
Elastic Slope (N/rad) x 1000	1431	2083	2023	2173
Maximum Load / Limit Load	0.976	1.26	1.18	1.195
Plastic Angle (Strain) on Low Cycle Fatigue (rad)				
Forward	0.106	0.069	0.079	0.095
Reverse	0.086	0.065	0.064	0.100
2nd Cycle Lim. Load (Percent of Max.)	89.2%	96%	89.3%	93.3%
Crack Initiation (rad)	0.088	0.069	0.079	0.082
Maximum Mean Normal Stress (σ/k)	2.75	2.2	1.78	2.78
Norm. Structural Crack Growth Ductility (d_{UP}/h_0)/(dP/P_{max})				
	0.576	0.575	0.752	
Structural Crack Growth Ductility (d_{UP}/dP) $\times 10^{-5}$ (Eq. 17)	-26.56	-7.94	-5.94	-7.66
Local Crack Growth Ductility (D_g) Eqs. (22) (36)	0.180	0.042	0.604	0.780

TABLE 6a. Ambient temperature mechanical properties of HY-100 steel.

Composition:	0.20% C, 2.25-3.50% Ni, 0.10-0.40% Mn, 0.15-0.35% Si			
Properties:	Yield Strength MN/m ²	Tensile Strength MN/m ²	Hardness HBN kgf/mm ²	Reduction in area %
	693	772	195	68.6

TABLE 6b. Experimental results

(l/h = 2.0)	Sym.	Asymmetrical		
(g/h)		0.0	0.0	0.5
ligament size (mm)	11.68	12.2	11.68	12.2
Elastic Slope (N/rad) x 1000	1929	2314	2133	2462
Maximum Load / Limit Load	1.019	1.289	1.269	1.177
Plastic Angle (Strain) on Low Cycle Fatigue (rad)				
Forward	0.05	0.069	0.071	0.06
Reverse	0.036	0.039	0.04	0.06
2nd Cycle Max. Load (Percent of Max.)	91.1%	91%	98%	93.4%
Crack Initiation (rad)	0.031	0.048	0.05	0.057
Maximum Mean Normal Stress (σ/k)	2.75	2.2	2.2	1.78
Norm. Structural Crack Growth Ductility (d_{up}/h_0)/dP/Pmax)		0.998	0.825	1.30
Structural Crack Growth Ductility (d_{up}/dP) $\times 10^{-5}$ (Eq.17)	-19.63	-12.16	-10.15	-14.21
Local Crack Growth Ductility (D_g) Eqs. (22) (36)	0.183	0.072	0.060	1.37

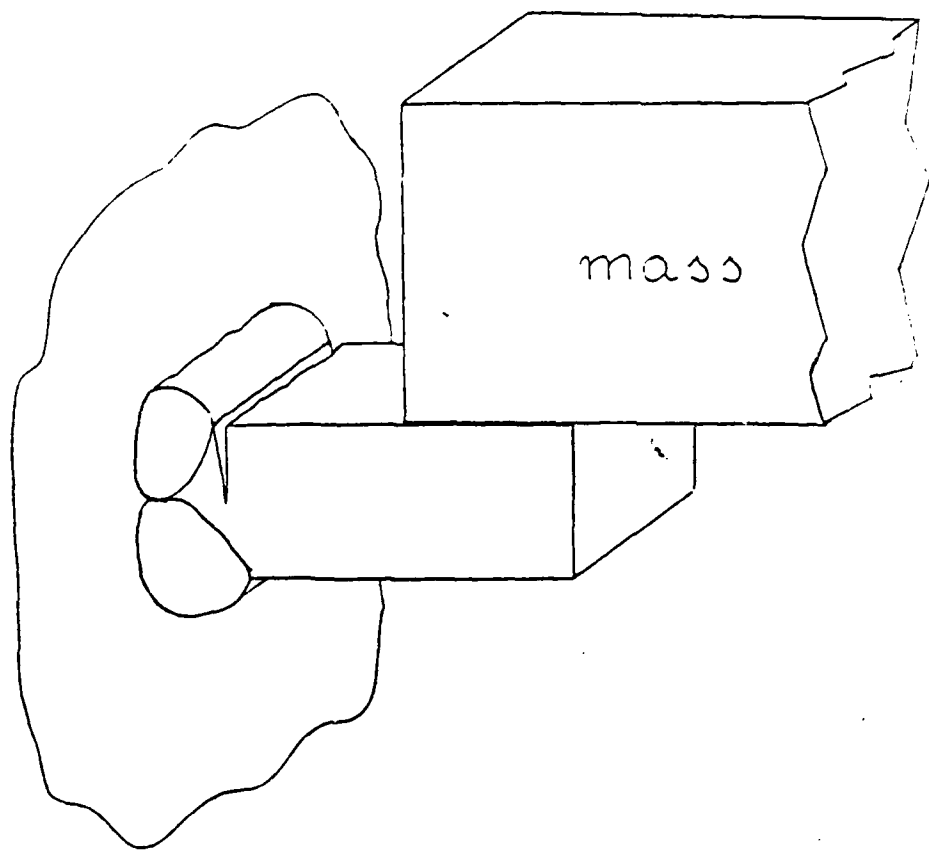


Figure 1. Typical example of an asymmetrically grooved rectangular bar under bending.

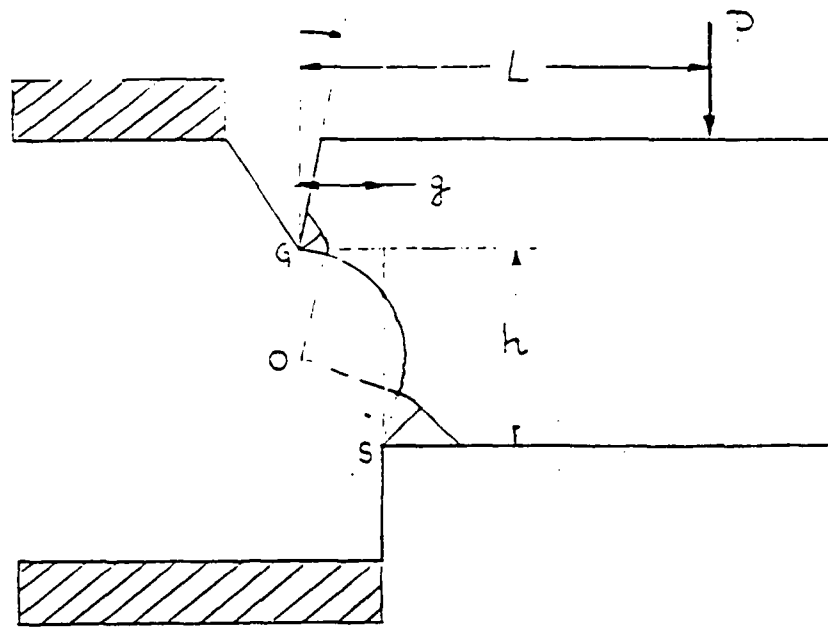


Figure 2a. General slipline field for an asymmetrically grooved cantilever bar.

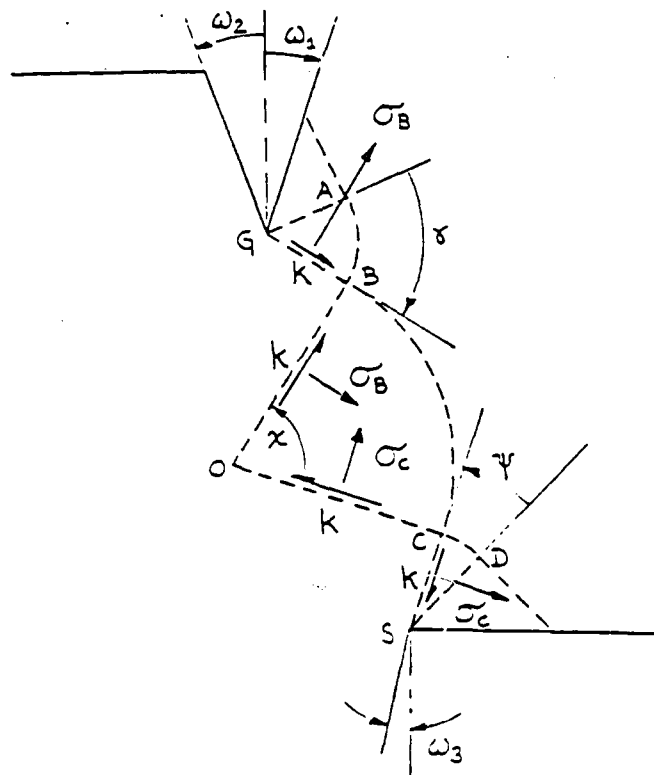


Figure 2b. Free body diagram of the general slipline field.

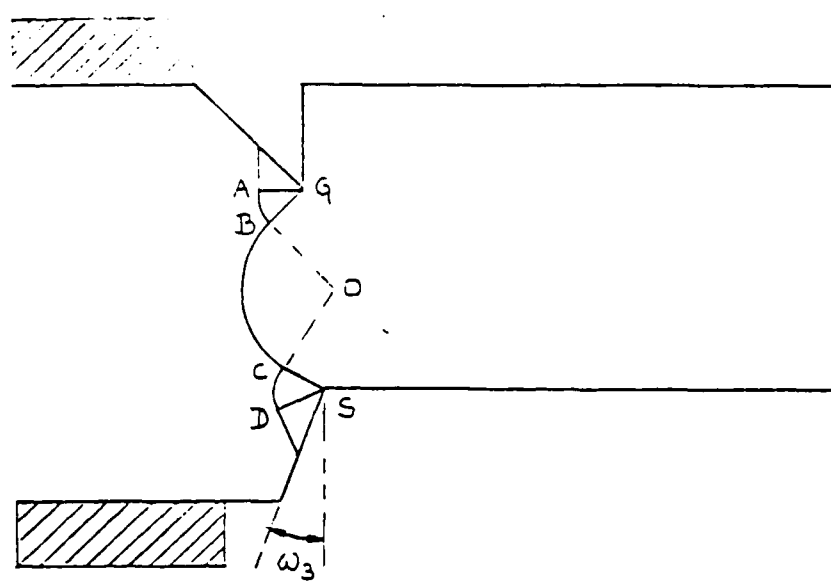


Figure 2c. Slipline field for a cantilever loaded bar with shoulder deformation.

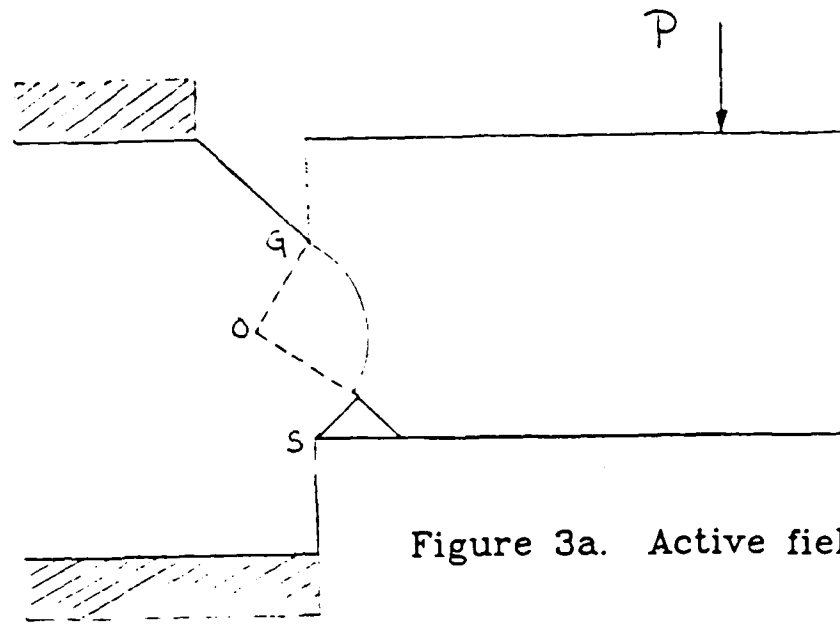


Figure 3a. Active field.

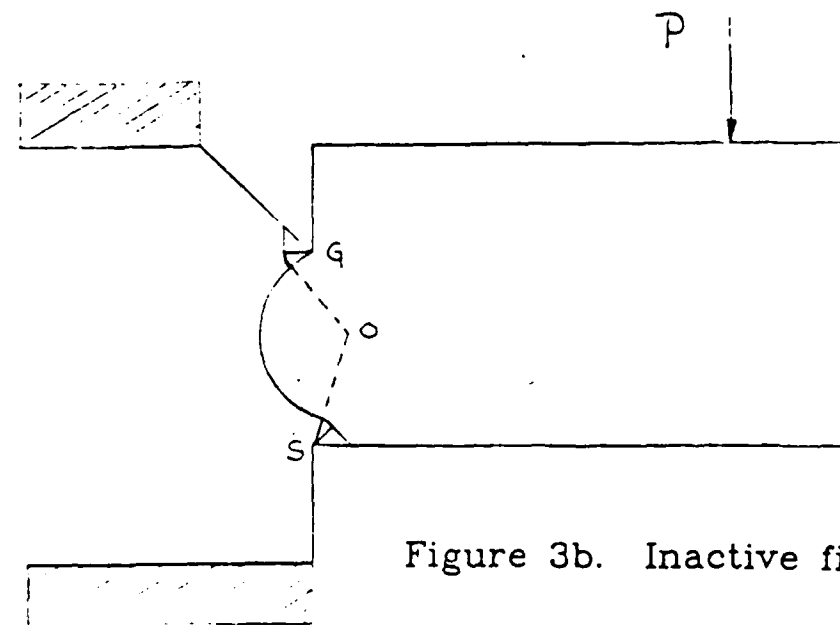


Figure 3b. Inactive field.

Figure 3. Slipline fields for a cantilever loaded bar.

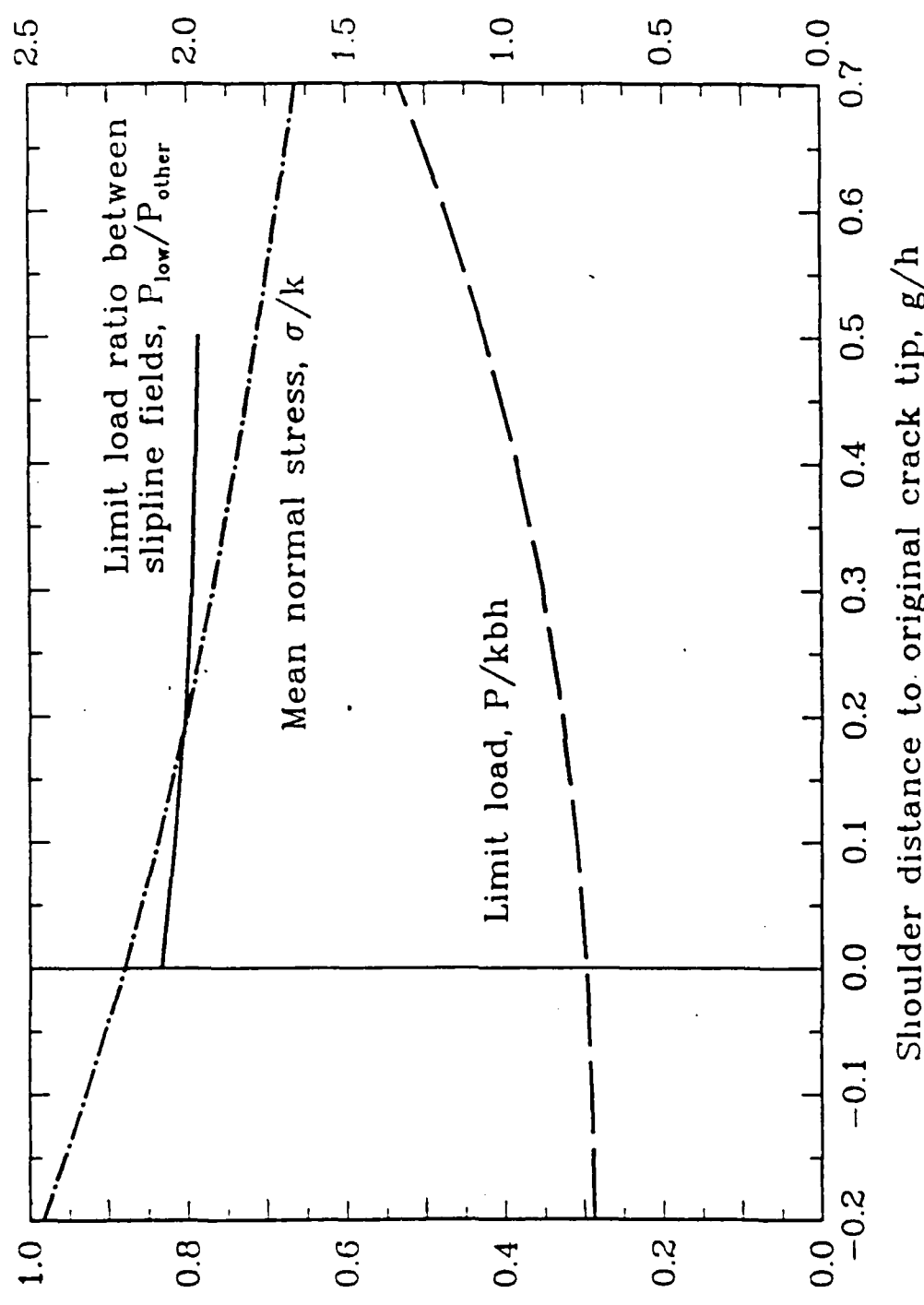


Figure 4a. Norm. load and stress for a cantilever bar as a function of shoulder distance to crack tip, g/h @ $L/h=2$

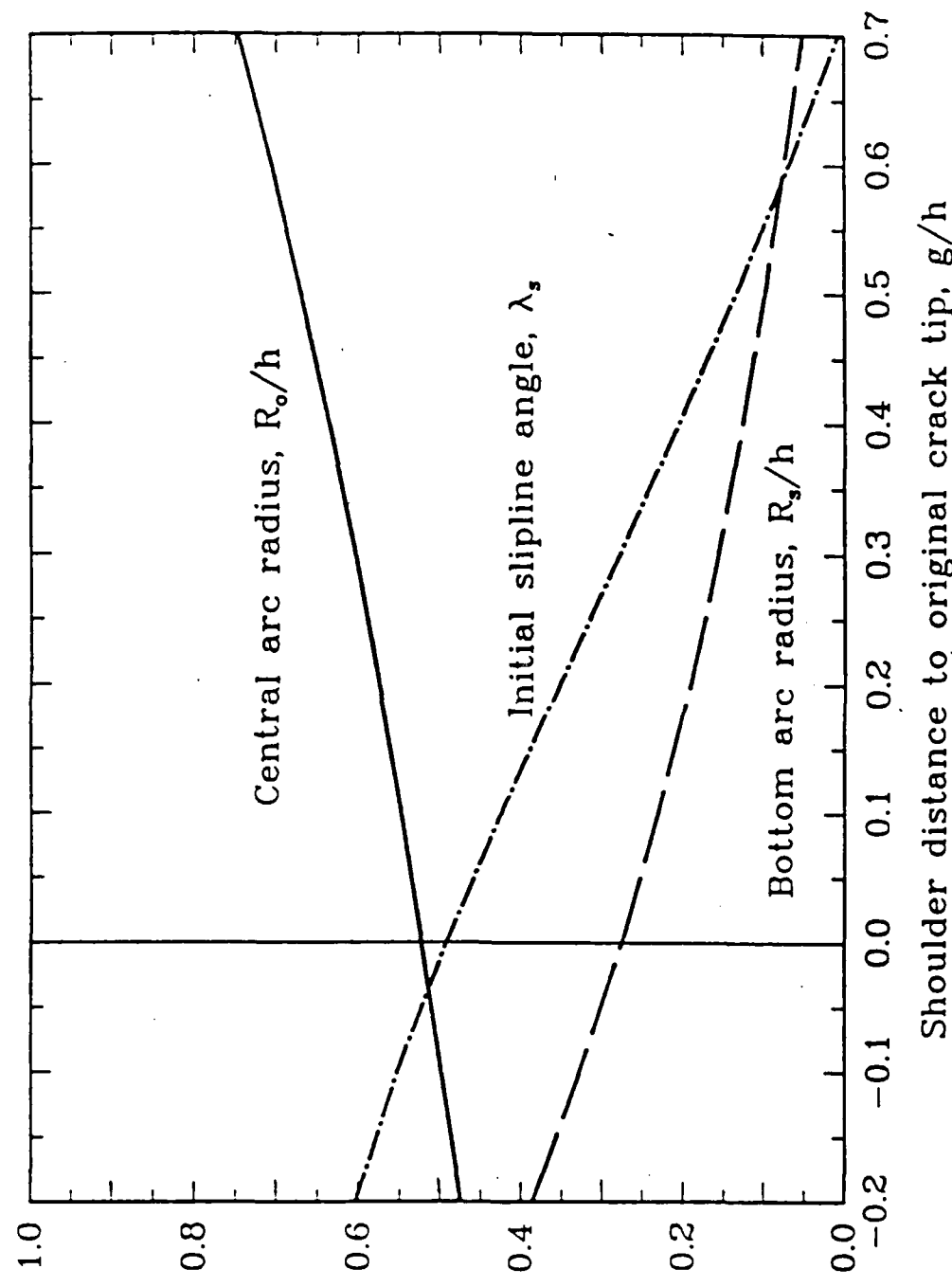


Figure 4b. Normalized radii for a cantilever bar as a function of shoulder distance to crack tip, g/h @ $L/h=2$

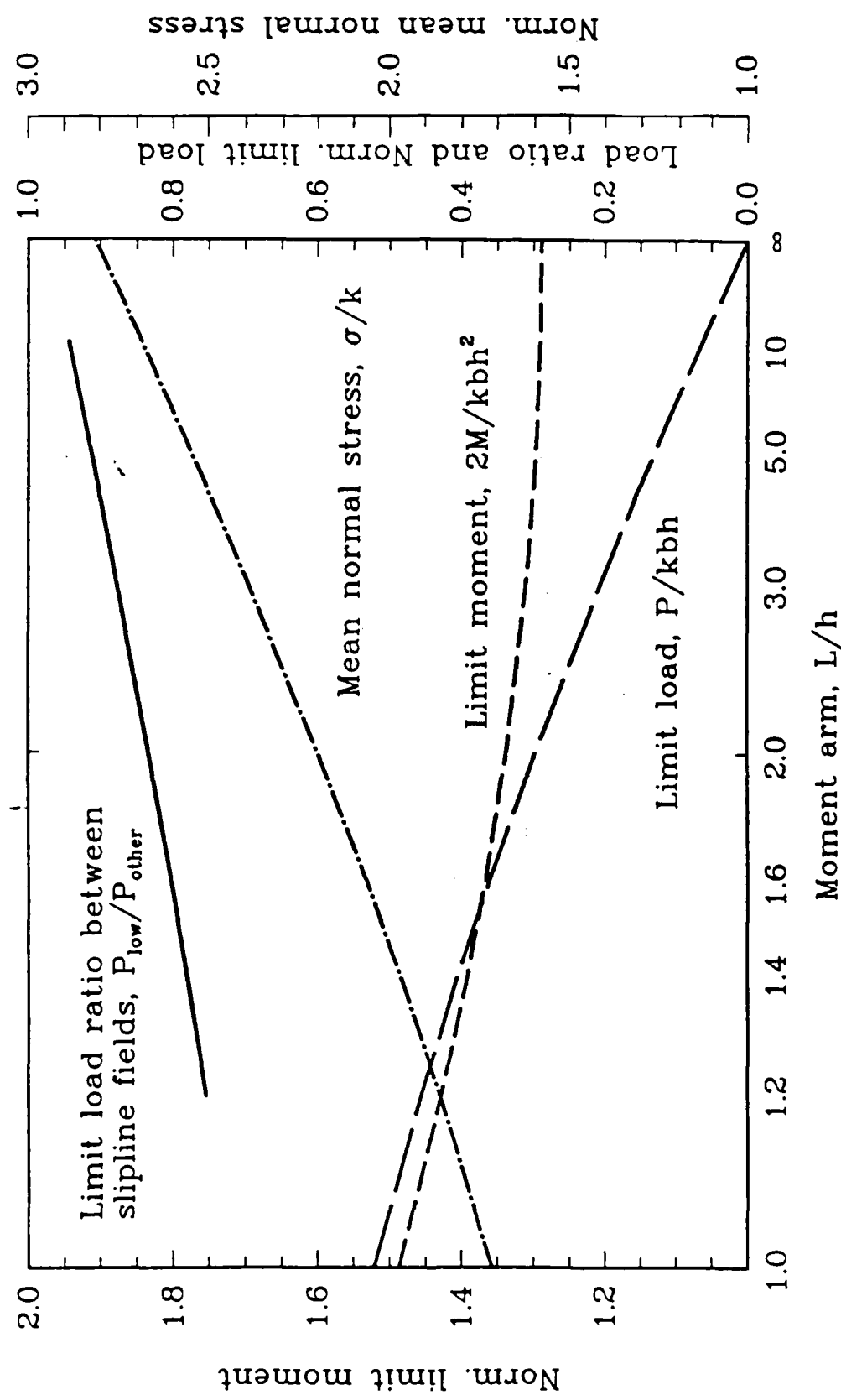


Figure 5a. Norm. load and stress for a cantilever bar as a function of moment arm, L/h @ $g/h=0$

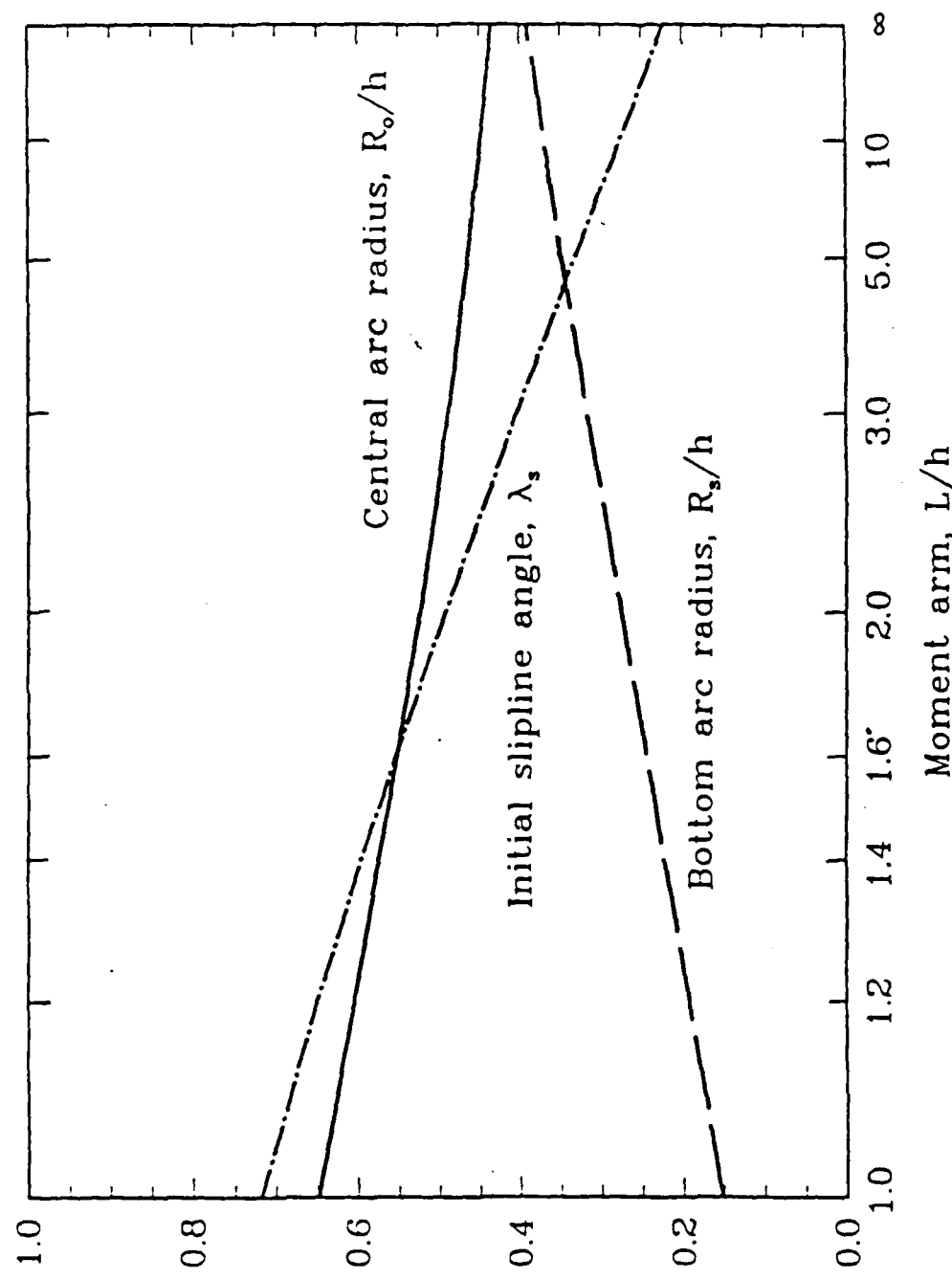


Figure 5b. Normalized radii for a cantilever bar as a function of moment arm, L/h @ $g/h=0$

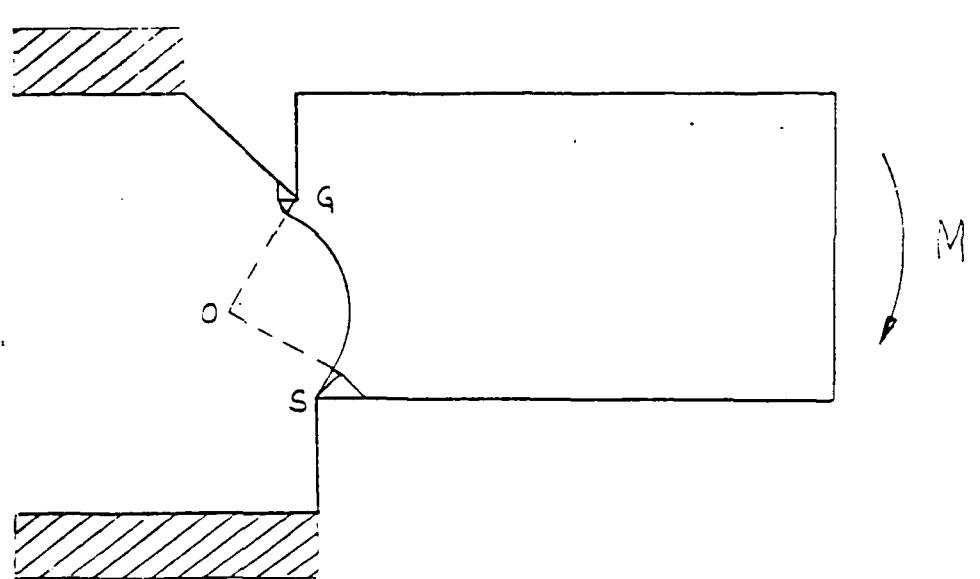
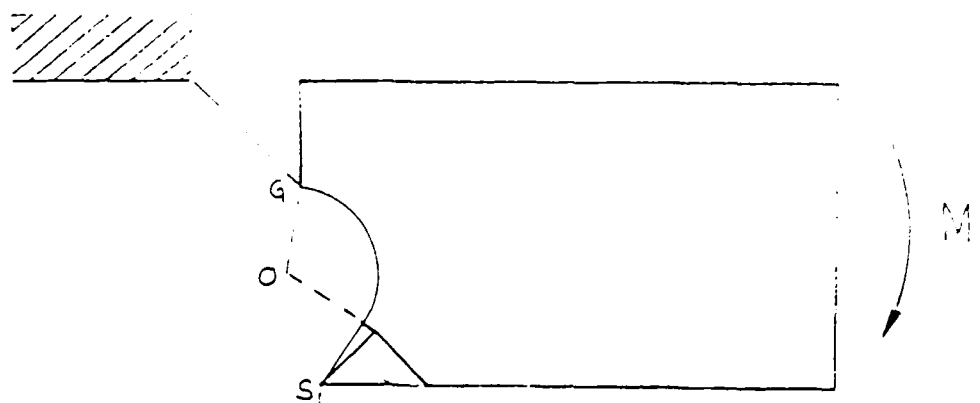


Figure 6. Slipline fields for an asymmetrically grooved bar under bending.

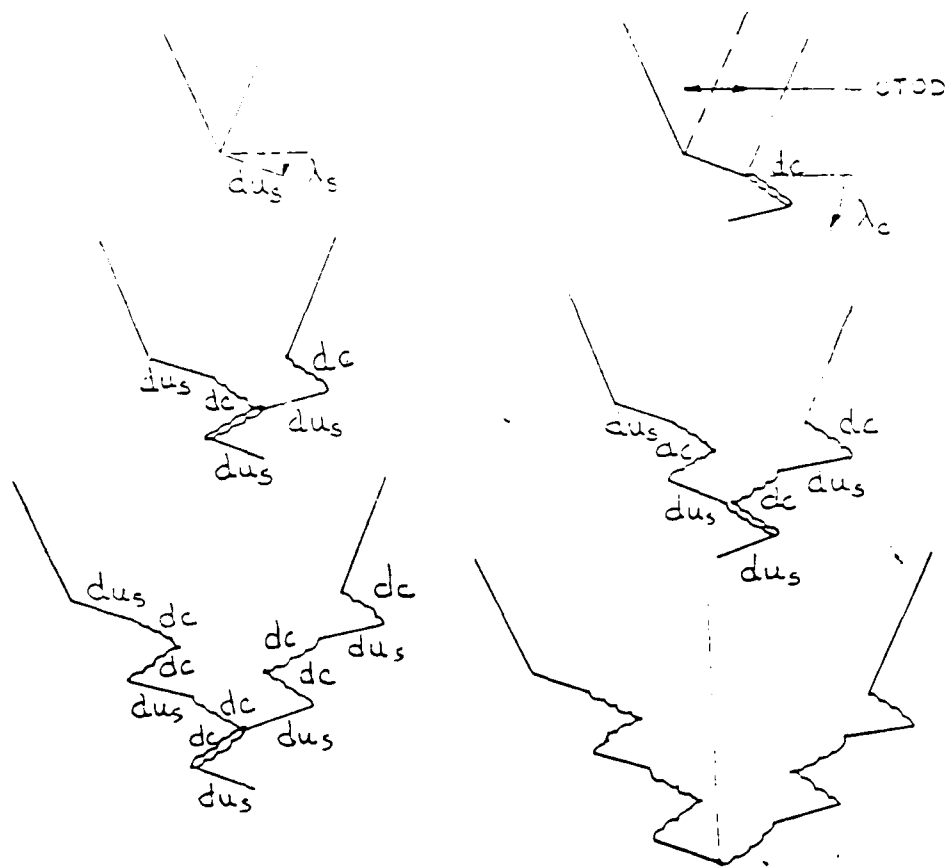


Figure 7a. Crack tip opening displacement, (CTOD), process on a symmetrically grooved/loaded specimen under two active sliplines.

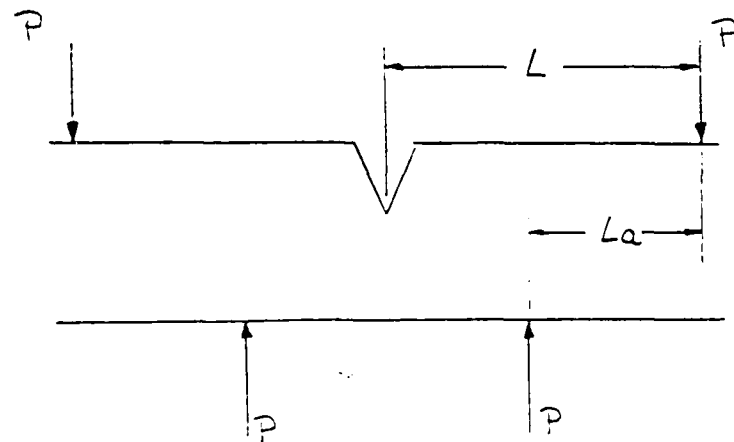


Figure 7b. General geometry

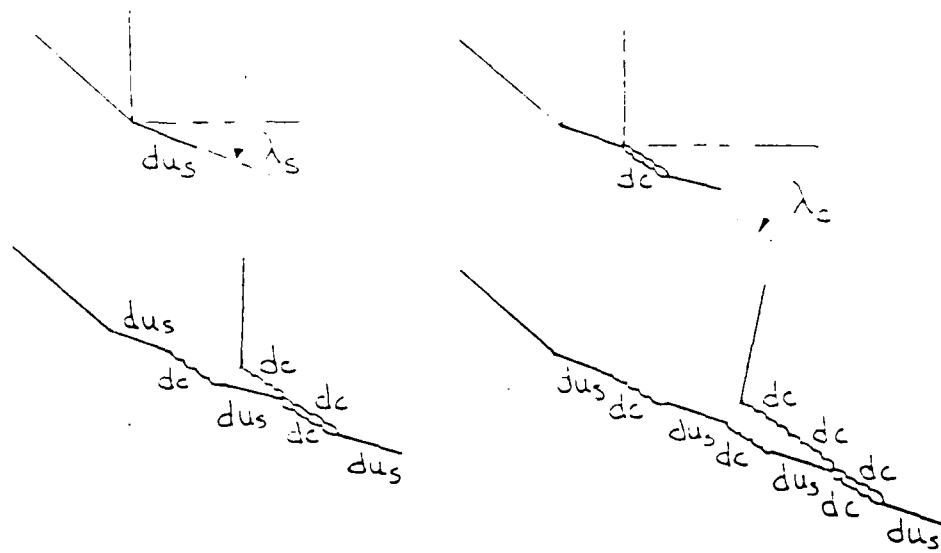


Figure 8a. Crack growth process in asymmetrically grooved cantilever specimens.

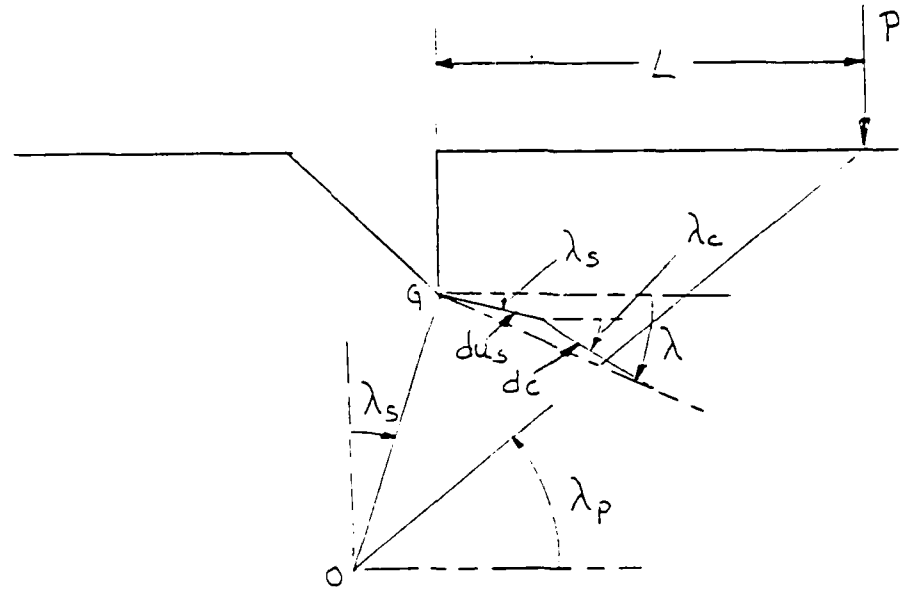


Figure 8b. Relation between general direction, λ , slip angle, λ_s , and fracture angle, λ_c .

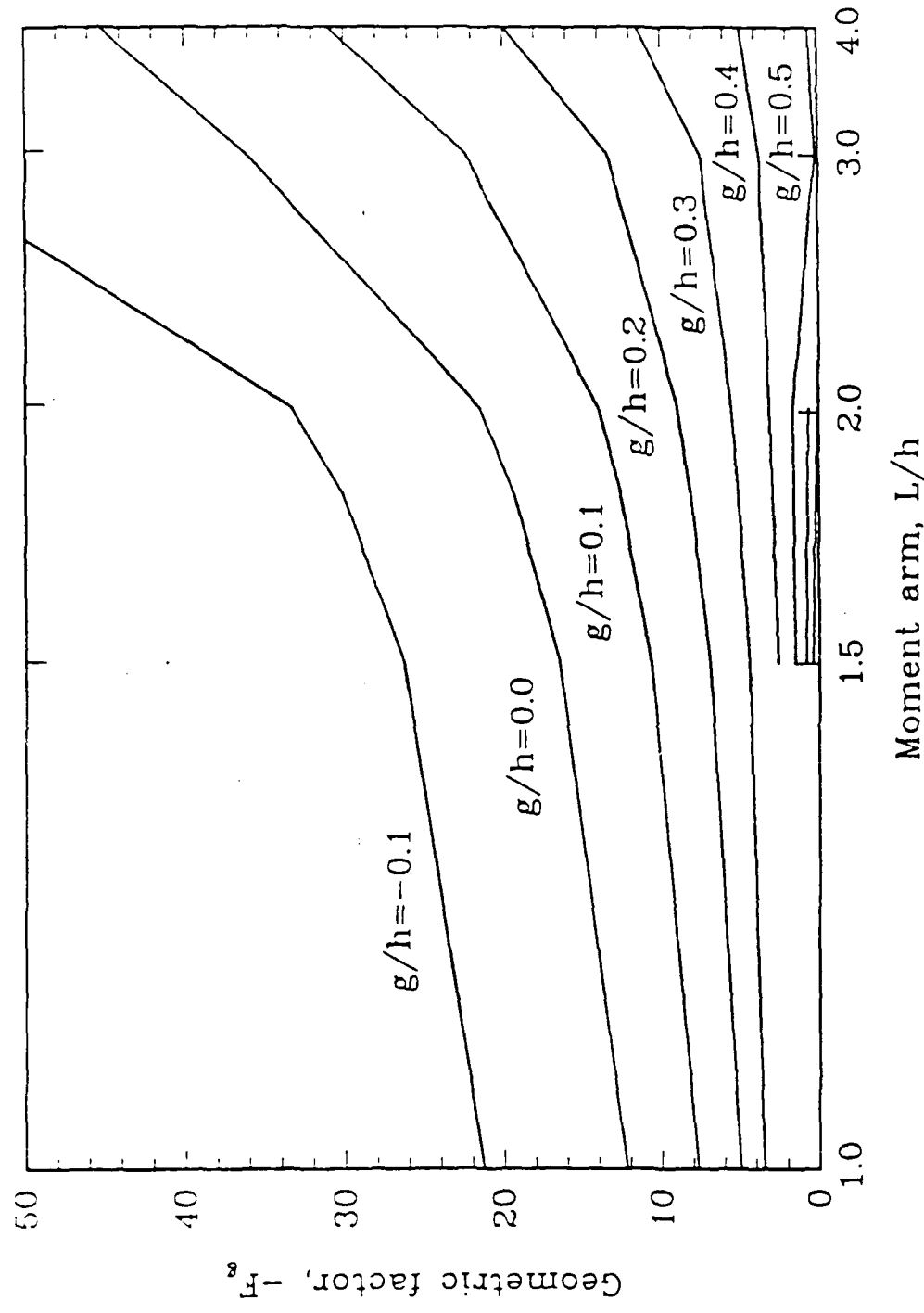


Figure 9. Geometric factor, F_g vs. moment arm, L/h

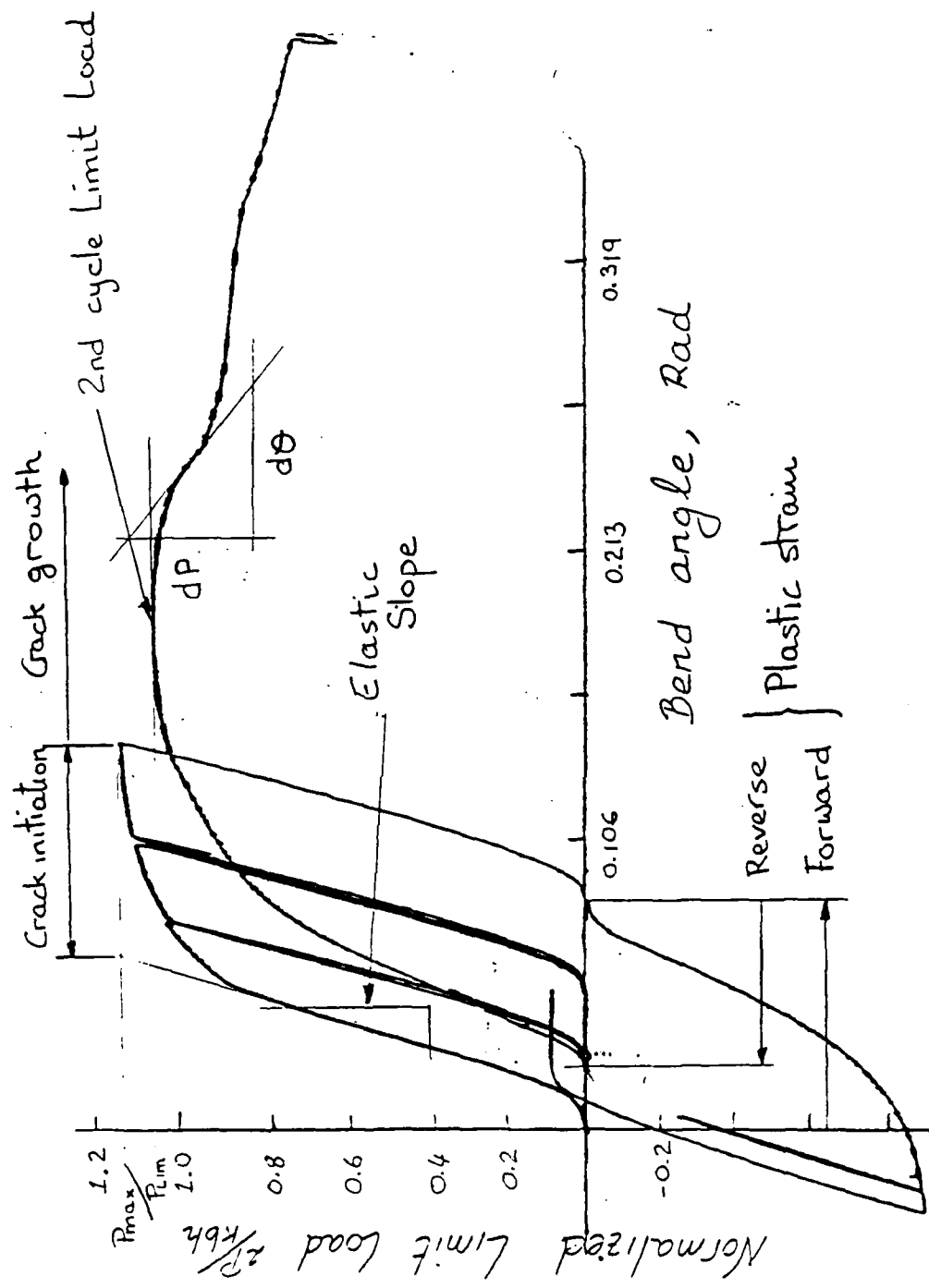


Figure 10. Typical load-displacement curve of bending experiments.

F

V

D

D T J C

9 —

86